Article

Pressure-Induced Structural Phase Transitions in the Chromium Spinel LiInCr$_4$O$_8$ with Breathing Pyrochlore Lattice

Meera Varma [1], **Markus Krottenmüller [1]**, **H. K. Poswal [2],*** and **C. A. Kuntscher [1],***

1   Experimentalphysik II, Augsburg University, 86159 Augsburg, Germany
2   High Pressure & Synchrotron Radiation Physics Division, Bhabha Atomic Research Centre, Trombay, Mumbai 400085, India
*   Correspondence: himanshu@barc.gov.in (H.K.P.); christine.kuntscher@physik.uni-augsburg.de (C.A.K.)

Abstract: This study reports high-pressure structural and spectroscopic studies on polycrystalline cubic chromium spinel compound LiInCr$_4$O$_8$. According to pressure-dependent X-ray diffraction measurements, three structural phase transitions occur at ∼14 GPa, ∼19 GPa, and ∼36 GPa. The first high-pressure phase is indexed to the low-temperature tetragonal phase of the system which coexists with the ambient phase before transforming to the second high-pressure phase at ∼19 GPa. The pressure-dependent Raman and infrared spectroscopic measurements show a blue-shift of the phonon modes and the crystal field excitations and an increase in the bandgap under compression. During pressure release, the sample reverts to its ambient cubic phase, even after undergoing multiple structural transitions at high pressures. The experimental findings are compared to the results of first principles based structural and phonon calculations.

Keywords: high-pressure studies; Raman spectroscopy; infrared spectroscopy; X-ray diffraction

1. Introduction

The chromium spinels ACr$_2$O$_4$ belong to the widely studied geometrically frustrated systems, owing to their varied magnetic couplings, magnetostructural transitions, and exotic ground states. With the A-site occupied by a non-magnetic ion, the magnetic chromium ions (Cr^{3+}) at the B-site form a network of corner-linked Cr$_4$ tetrahedra, i.e., the pyrochlore lattice. The dominant antiferromagnetic (AFM) interactions between the Cr^{3+} ions in the pyrochlore network leads to strong magnetic frustrations, which result in Jahn–Teller-driven structural distortion and antiferromagnetic ordering at low temperatures. Due to their varied response to external parameters, the chromium-based spinels could be used in magnetic sensing devices, data storage or spintronic devices [1]. There have also been studies reporting their use as a potential electrode support material [2]. A study also suggested cobalt containing chromium spinels as possible candidates for catalytic combustion [3].

An archetype derived by substituting two different ions at the A-site of ACr$_2$O$_4$ was first reported by Joubert and Durif in 1966 [4]. The difference in ionic radii at the A-site led to an alternate arrangement of small and large Cr$_4$ tetrahedra at the B-sites, known as the breathing pyrochlore lattice (see Figure 1) [5–8]. This new family of Cr spinels, namely LiMCr$_4$O$_8$ (with M = In, Ga, Fe), are being actively investigated due to the geometrical frustration and the Cr–Cr bond alternations in these materials. The substitution of different ions at the A-site leads to the loss of inversion symmetry found in the conventional spinels, and the crystal symmetry is reduced to F$\bar{4}$3m. The alternating smaller and larger Cr–Cr bonds between Cr$_4$ tetrahedra also cause a difference in the nearest-neighbour magnetic interactions, without relieving the frustration in the system. The magnitude of AFM interactions between neighbouring Cr ions is denoted as J and J′ for small and large tetrahedra, respectively. The ratio of J and J′ is defined as the breathing factor B$_f$, i.e., B$_f$ = J′/J, and determines the degree of frustration in the system [5].

The physical properties of this family of frustrated breathing pyrochlores $LiMCr_4O_8$ (with M = In, Ga, Fe) are highly dependent on the cationic radii at the A-site, which define the breathing factor and in turn have an overwhelming influence on the response of the material to different thermodynamic conditions. Recent studies have been conducted to improving the understanding of the structural and magnetic response of these materials at low temperatures. A temperature-dependent neutron diffraction experiment on $LiInCr_4O_8$ indicated the opening of a spin gap below 65 K, which is followed by a long-range magnetic ordering at $\sim$15.9 K [5]. An NMR study on $LiInCr_4O_8$ suggested a singlet ground state with a gap at 18 K and a structural transition at 16 K followed by a second-order AFM transition at 13 K [6]. However, another study reported a structural transition at 18 K followed by magnetic ordering at 12 K [7]. The related compound $LiGaCr_4O_8$ has been reported to show short-range AFM ordering close to $\sim$50 K, which is followed by a first-order magnetostructural transition around $\sim$15 K [5,6]. However, another study reported it as two consecutive events of magnetic and structural transitions at 14.1 K and 14.5 K, respectively, [8]. As opposed to $LiInCr_4O_8$ and $LiGaCr_4O_8$, the compound $LiFeCr_4O_8$ has been reported to undergo a ferrimagnetic transition at 94 K. Furthermore, the opening of a spin gap at $\sim$60 K and a magnetostructural transition at $\sim$23 K were found [9]. It is to be noted that all three compounds, having different degrees of frustration, show a structural instability at low temperature.

Although low-temperature-induced structural and magnetic responses have been explored and reported for this class of compounds, high-pressure studies have not been reported to the best of our knowledge. In this work, we study the structural phase transitions in $LiInCr_4O_8$ induced by high pressure using synchrotron-based X-ray diffraction (XRD) and Raman and infrared (IR) spectroscopic measurements supplemented by density functional theory (DFT)-based simulations.
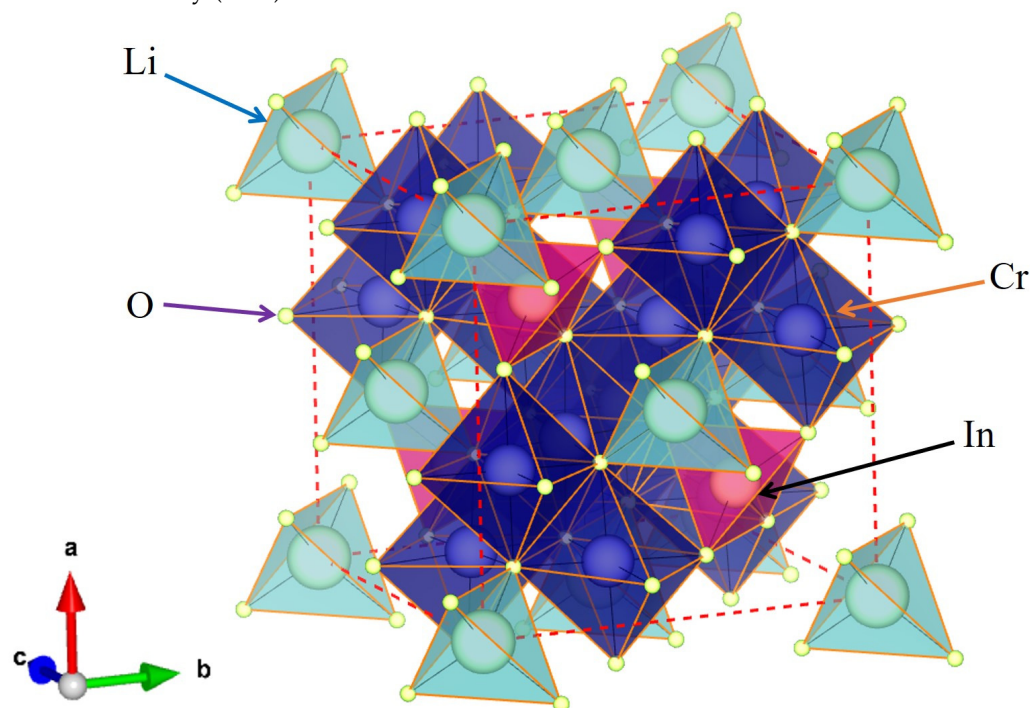
Figure 1. Sketch of the breathing chromium spinel $LiInCr_4O_8$ crystal structure with LiO_4 and InO_4 tetrahedra and CrO_6 octahedra as structural units.

2. Materials and Methods

Polycrystalline $LiInCr_4O_8$ was synthesized using the solid-state reaction method reported previously [5,8], where the stoichiometric amounts of In_2O_3 and Cr_2O_3 and 10% excess of Li_2CO_3 were thoroughly ground, pelleted, and heated in a furnace at 1100 °C for 48 h in an alumina crucible with intermittent grinding. As lithium is volatile, a slow rate of

cooling was maintained. The phase purity of the synthesized compound $LiInCr_4O_8$ was characterized using XRD measurements performed in the angle-dispersive mode at the ECXRD beamline (BL-11), Indus-2, RRCAT. X-rays with energies of 19.7 keV ($\lambda = 0.6280$ Å) were incident on the synthesized polycrystalline sample. NIST standard LaB_6 was used to calibrate the distance from sample to detector.

High-pressure XRD (HPXRD) measurements on $LiInCr_4O_8$ were performed at the XPRESS beamline of the Elettra synchrotron radiation source, Italy. Powdered sample was loaded into a Mao–Bell type diamond anvil (DAC) along with gold (Au) as a marker to determine the pressure with an accuracy of $\sim$0.1 GPa. [10,11]. The diamonds had a culet diameter of $\sim$400 μm. A tungsten gasket of thickness $\sim$180 μm was pre-indented to a thickness of $\sim$50 μm before drilling a hole of 150 μm at the centre of the gasket. A methanol–ethanol mixture in a 4:1 ratio served as a quasi-hydrostatic pressure transmitting medium (PTM) [12]. Monochromatic X-rays of energy 25 keV ($\lambda = 0.4957$ Å) were incident on the sample. A MAR345 detector was used to record the diffraction patterns. Standard LaB_6 loaded in the DAC was used to calibrate the experimental setup. The diffraction images were reduced into 2θ-intensity patterns using the program Fit2D [13], and the refinement of the XRD patterns obtained were performed using GSAS [14].

Raman spectroscopy measurements were performed with a confocal micro-Raman setup (Jobin–Yvon T64000 spectrograph, single stage mode, 1800 groves/mm grating, and a resolution of 2 cm^{-1}) using a $50\times$ objective in the back scattering geometry. A 488 nm argon ion laser was used as excitation source. The pressure-dependent Raman scattering measurements were carried out using a gas membrane type DAC, with diamonds with $\sim$500 μm culet diameter. The pressure inside the DAC was monitored using the well-known ruby fluorescence shift with an accuracy of 0.1 GPa [15]. A methanol–ethanol mixture in a 4:1 ratio was used as PTM.

The infrared spectroscopic measurements were performed using a Bruker Vertex FTIR spectrometer coupled to an IR microscope (Bruker Hyperion). The ambient pressure infrared reflectivity measurements were carried out in the spectral range 100–25,000 cm^{-1} on a polycrystalline sample pressed into a pellet of thickness 72 μm. The resolution for the various frequency ranges, viz., FIR, MIR, NIR-VIS, amount to 2 cm^{-1}, 4 cm^{-1}, and 8 cm^{-1}, respectively. Reflection from an aluminium mirror was used for the reference measurement, for normalizing the sample spectrum. The optical conductivity σ_1 was obtained by Kramer–Kronig (KK) transformation. For the KK transformation, the reflectivity spectrum was fitted with the Lorentz model and extrapolated to zero frequency based on the fitting model; in the high-energy range, a constant extrapolation up to 10^5 cm^{-1} was used, and beyond this, an extrapolation following a $1/w^4$ dependency was chosen.

For the pressure-dependent infrared transmittance measurements in the spectral range 500–20,500 cm^{-1} with a resolution of 4 cm^{-1}, the powder sample was diluted with CsI in the ratio 1:20 and pressed into a pellet of thickness 64 μm. A small piece of this diluted pellet was loaded into a membrane type DAC (500 μm culets) along with ruby spheres and well-ground CsI powder serving as reference for normalizing the sample spectrum while at the same time acting as a quasihydrostatic PTM [16]. The absorption spectrum was calculated using the formula $A = -\log_{10}(T)$, where A is the absorbance and T is the measured transmittance spectrum.

Ab initio-based simulations for structural relaxations were performed using DFT within the framework of the projected augmented wave (PAW) method [17], as implemented in the Quantum Espresso 6.4.1 package [18]. Calculations were performed using Perdew, Burke, and Ernzerhof (PBE) [19] generalized gradient approximations (GGA) for exchange and correlation functional. Structural relaxations were performed on a primitive cell of $LiInCr_4O_8$ with fourteen atoms of four different types in a non-magnetic configuration. Simulations were performed by considering one valence electron of Li ($2s^1$), thirteen valence electrons of In ($5s^2\ 5p^1\ 4d^{10}$), six valence electrons of Cr ($4s^2\ 3d^4$), and six valence electrons of O ($2s^2\ 2p^4$). A plane wave cut-off energy of 160 Ry was used for expanding the basis set. The Brillouin zone integration was performed at the zone centre on a $6 \times 6 \times 6$ Monkhorst–

Pack k-point mesh [20]. The Hellman–Feynman forces were converged until the largest force component was less than 1×10^{-5}. For the purpose of phonon-mode assignments, density functional perturbation theory (DFPT) [21] calculations were performed using Martins–Trouilier [22] pseudopotentials with local density approximation (LDA) on the primitive lattice of $LiInCr_4O_8$ at ambient volume.

3. Results

3.1. Ambient Pressure Results

$LiInCr_4O_8$ crystallizes in the cubic space group $F\bar{4}3m$ with four formula units per unit cell [5]. The lattice parameter, shape profile parameters, and asymmetry corrections were refined during the Rietveld refinement of the ambient pressure XRD pattern, shown in Figure 2. The background was fitted using a Chebyschev polynomial. The synthesized sample contains less than 2% unreacted Cr_2O_3 as observed from Figure 2. The refined lattice parameter is $a = 8.4038(1)$ Å and the unit cell volume amounts to V = 593.52(2) Å^3, with $R_p = 0.075$ and $R_{wp} = 0.109$. These values are in good agreement with the reported values of $a = 8.4205$ Å and V = 597.05 Å^3 [4,5]. The fractional coordinates, occupations, and Wyckoff sites as reported by an earlier study [5] and the refined thermal parameter obtained from the Rietveld analysis are given in Table 1.
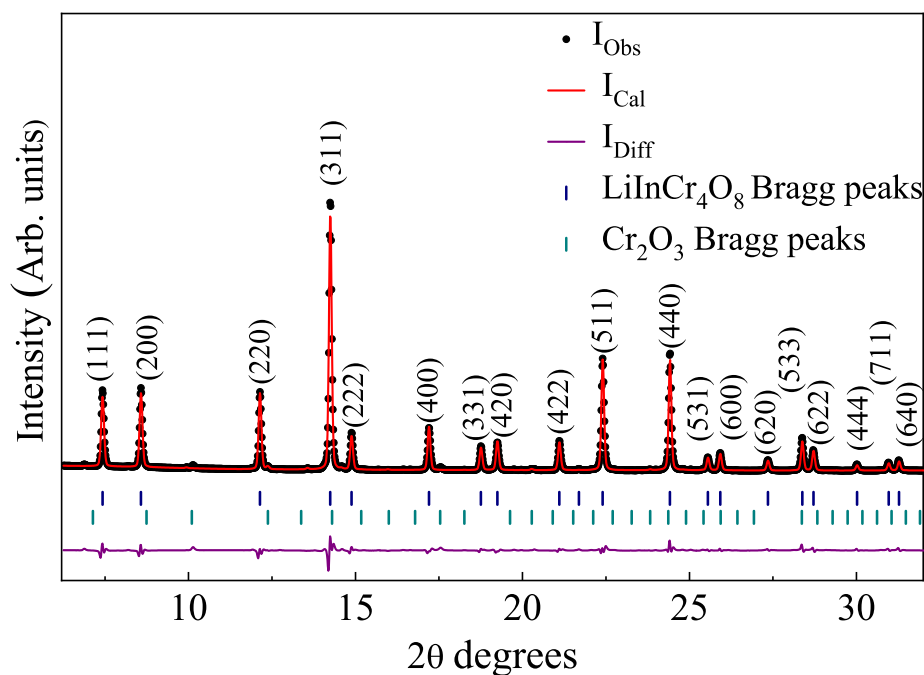

Figure 2. Rietveld refinement of the X-ray diffraction pattern of $LiInCr_4O_8$ at ambient pressure.

Table 1. The Wyckoff sites, fractional coordinates, and occupations as reported in an earlier study [5] and thermal parameter U as obtained from Rietveld refinement of $LiInCr_4O_8$ at ambient conditions. Space group $F\bar{4}3m$, Z = 4, a = 8.4038(1) Å, V = 593.52(2) Å^3.

Atoms	Wyckoff Sites	x	y	z	Occupancy	U
Li1	4a	0.0000	0.0000	0.0000	0.9920	1.090
In1	4a	0.0000	0.0000	0.0000	0.0080	0.350
Li2	4d	0.7500	0.7500	0.7500	0.0080	1.090
In2	4d	0.7500	0.7500	0.7500	0.9920	0.350
Cr	16e	0.3719	0.3719	0.3719	1.0000	0.140
O1	16e	0.1377	0.1377	0.1377	1.0000	0.380
O2	16e	0.6107	0.6107	0.6107	1.0000	0.180

DFT-based simulations were performed using LDA and GGA pseudopotentials and the results for ambient volume calculations are compared in Table 2. The *A*-site cations Li^{1+} and In^{3+} at 4a and 4d crystallographic sites form LiO_4 and InO_4 tetrahedra, respectively, and share corners with CrO_6 at the B-site (see Figure 1). The CrO_6 octahedral units at the general 16e Wyckoff positions have shared edges between them, and the Cr_4 tetrahedra form the breathing pyrochlore lattice. The Cr–Cr distances are usually short enough to facilitate electron hopping in some of the conventional spinels (Mott insulators). The quality of synthesized sample was verified by determining the degree of distortion (d′/d) due to the two different Cr–Cr bond lengths of Cr_4 tetrahedra from the Rietveld refinement, where the ratio d′/d is found to be 1.051, which matches with the reported value [4,5,8]. This ratio of dissimilar Cr–Cr distances can be directly associated with the breathing factor B_f in $LiInCr_4O_8$.

Table 2. Comparison of experimental and theoretical primitive cell volume together with the distortion parameter and the reported values from the literature.

	Reported from [5]	Present Study	Simulations	
			LDA	GGA
Volume of Primitive cell ($Å^3$)	149.24	148.38	149.9925	149.0278
distortion parameter (d′/d)	1.051	1.05	1.32	1.33

For a primitive cell containing one formula unit (14 atoms), the factor group analysis gives the following irreducible representations:

$$\Gamma_{total} = 3A_1 + 3E + 3T_1 + 8T_2.$$

This can further be classified as:

$$\Gamma_{acoustic} = T_2$$

$$\Gamma_{IR} = 7T_2$$

$$\Gamma_{Raman} = 3A_1 + 3E + 7T_2$$

From the expected 13 Raman-active modes at ambient conditions, we experimentally observe nine modes, which are denoted as M_1, M_2, ... M_9 in Figure 3. Due to the loss of inversion symmetry in comparison with conventional spinels, $LiInCr_4O_8$ has T_2 modes which are both IR- and Raman-active. The weak mode at ~530 cm^{-1} has been assigned to Cr_2O_3 [23,24]. The peak observed at ~220 cm^{-1} is a plasma line from the excitation source used, which served as an internal calibrant. The ambient pressure Raman spectrum of $LiInCr_4O_8$ in Figure 3 matches well with a recently reported study [25], except for the low-energy Raman mode M_1, which is not observed in the recorded spectral range of Ref. [25]. Because there has been no detailed report on the vibrational properties of $LiInCr_4O_8$, DFPT calculations were carried out for explicit assignment of Raman and IR modes. These calculations were performed on a primitive cell consisting of 14 atoms using the Martins–Trouilier pseudopotentials with LDA approximations. The phonon modes were assigned with the help of Molden, a visualization software [26]. Simulations were also performed using PAW potentials with GGA approximations at ambient volume. The theoretical results are compared with experimental findings, summarized in Table 3.

Predominantly, the observed Raman modes can be classified as the internal vibrations of polyhedral units (viz., LiO_4, InO_4 and CrO_6). Due to the covalent nature of In–O and Cr–O bonds, they are expected to have stronger contributions in the Raman spectrum. The

symmetry of a free CrO_6 ion is reduced inside the crystal site. Table 4 shows the changes in the internal modes of a free CrO_6 ion at the crystal site (C3v) of the ambient pressure cubic phase (T_d). Of these CrO_6 modes, only the A_1 and T_2 modes are Raman active in $LiInCr_4O_8$.

From the DFPT calculations, the Raman-active T_2 mode observed at 164 cm^{-1} is assigned to the translation motion of In. The modes M_2 and M_3 at 310 cm^{-1} and 443 cm^{-1}, respectively, are both assigned to the translation motion of Li ions. The Raman modes at 460 cm^{-1} and 491 cm^{-1} (M_4 & M_5) are associated with asymmetric and symmetric O–Li–O bending vibrations, respectively. The strongest Raman mode observed at ∼590 cm^{-1} is related to the O–Cr–O symmetric bending and O–In symmetric stretching vibrations, whereas the adjacent T_2 mode at ∼582 cm^{-1} is related to the O–Cr–O asymmetric bending and In-O asymmetric stretching vibrations. In a recent study, the DFT-based calculations for $LiGaCr_4S_8$ show large differences in the calculated Cr–Cr distances in magnetic and non-magnetic configurations of the system [27]. This could explain the large difference in the calculated and observed M_6 and M_7 modes, as all the calculations are performed in a non-magnetic configuration in the present study. The Raman modes at 718 cm^{-1} and 739 cm^{-1} (M_8 and M_9) are assigned to asymmetric and symmetric stretching vibrations of Li–O. A study on $LiFeCr_4O_8$ has assigned the strongest observed mode to Cr–O stretching vibration [9]. However, as the CrO_6 octahedra have shared edges, they restrict the Cr–O stretching motion in this structure, and hence only the bending modes are prominent.
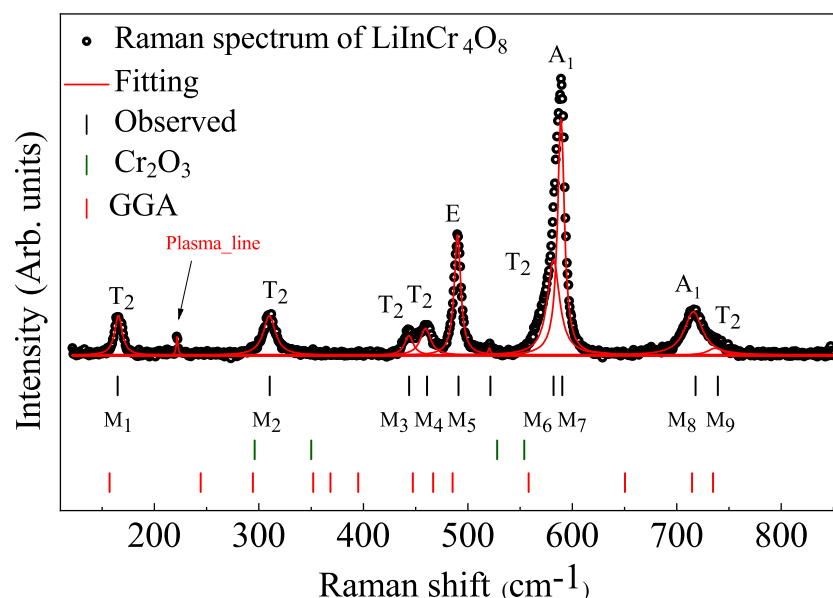

Figure 3. Ambient pressure Raman spectrum of $LiInCr_4O_8$, together with the fitting curve. Shown also are the theoretical mode frequencies (GGA) and the Raman mode frequencies for Cr_2O_3 [23,24].

Table 3. Mode assignment and comparison of experimental and theoretical mode frequencies (in cm^{-1}). (w), (m), and (s) denote the strength of active mode, viz., weak, medium and strong, respectively.

Modes Assigned		Raman			IR	
	Obs	LDA	GGA	Obs	LDA	GGA
T_2	165 (m)	160	157	-	160	157
E	-	245	244			
T_2	310 (m)	300	294	-	300	294
A_1	-	349	352			

Table 3. *Cont.*

Modes Assigned		Raman			IR		
	Obs	LDA	GGA	Obs	LDA	GGA
T_2	-	359	368	406	359	368
E	-	398	395			
T_2	444 (m)	471	447	473	471	447
T_2	461 (m)	475	467	529	475	467
E	491 (s)	503	485			
T_2	582 (m)	561	558	581	561	558
A_1	591 (s)	642	650			
A_1	718 (m)	731	715			
T_2	739 (w)	756	735	651	756	735

Table 4. Internal modes of CrO_6 octahedra.

Modes		Free CrO_6 Ion (O_h)		Site Symmetry (C_{3v})		Crystal Symmetry (T_d)
ν_1	$\rightarrow$	A_{1g}	$\rightarrow$	A_1	$\rightarrow$	A_1
ν_2	$\rightarrow$	E_g	$\rightarrow$	E	$\rightarrow$	E
ν_3	$\rightarrow$	F_{1u}	$\rightarrow$	A_1+E	$\rightarrow$	T_2
ν_4	$\rightarrow$	F_{1u}	$\rightarrow$	A_1+E	$\rightarrow$	T_2
ν_5	$\rightarrow$	F_{2g}	$\rightarrow$	A_1+E	$\rightarrow$	T_2
ν_6	$\rightarrow$	F_{2u}	$\rightarrow$	A_2+E	$\rightarrow$	T_1
ν_{rot}	$\rightarrow$	F_{1g}	$\rightarrow$	A_1+E	$\rightarrow$	T_2
ν_{tran}	$\rightarrow$	F_{1u}	$\rightarrow$	A_1+E	$\rightarrow$	T_2

Figure 4a depicts the ambient pressure reflectivity spectrum of $LiInCr_4O_8$ over a broad frequency range, together with the Lorentz fitting. The inset shows the low-frequency range up to 800 cm^{-1}, where the phonon modes are located. The corresponding optical conductivity σ_1 obtained from the KK transformation is depicted in Figure 4b. The σ_1 spectrum shows strong phonon contributions in the far-infrared range, which is followed by the onset of electronic excitations around ~0.1 eV, which gradually increases to two prominent absorption bands centred at ~1.65 and 2.4 eV. Based on previous studies, the absorption bands can be assigned to intra-atomic *d-d* excitations, i.e., crystal field (CF) excitations, of the Cr^{3+} ions in an octahedral environment. Electronic excitations from the $^4A_{2g}$ ground state to the $^4T_{2g}$ and $^4A_{1g}$ excited states are expected in the spectral ranges of ~13,000 to 17,000 cm^{-1} and ~13,000 to 17,000 cm^{-1}, respectively, and the spin-forbidden transitions from $^4A_{2g}$ to ^2E_g and $^2E_{2g}$ are expected in the spectral ranges of 13,000 to 14,400 cm^{-1} and 18,000 to 19,200 cm^{-1}, respectively, [28–36].

The inset in Figure 4b shows the observed ten phonon modes fitted with Lorentzian oscillators. However, the group theoretical analysis predicts only seven T_2 modes for LICO. Therefore, modes were assigned to the strongest modes after comparison with DFPT calculations to the closest calculated values (see Table 3). An earlier infrared spectroscopic study on $LiFeCr_4O_8$ has assigned the observed five phonon modes to the internal vibrations of the polyhedral units, viz., Li–O stretching modes in the range 400–500 cm^{-1} and CrO_6 and FeO_4 vibrations around 500 cm^{-1} and ~640 cm^{-1}, respectively [37]. In the present study, based on the DFPT calculations, the phonon modes above 600 cm^{-1} are assigned to the Li–O stretching vibrations. The low-energy modes are assigned to the In–O vibrations and those observed around ~500 cm^{-1} belong to the CrO_6 internal vibrations.
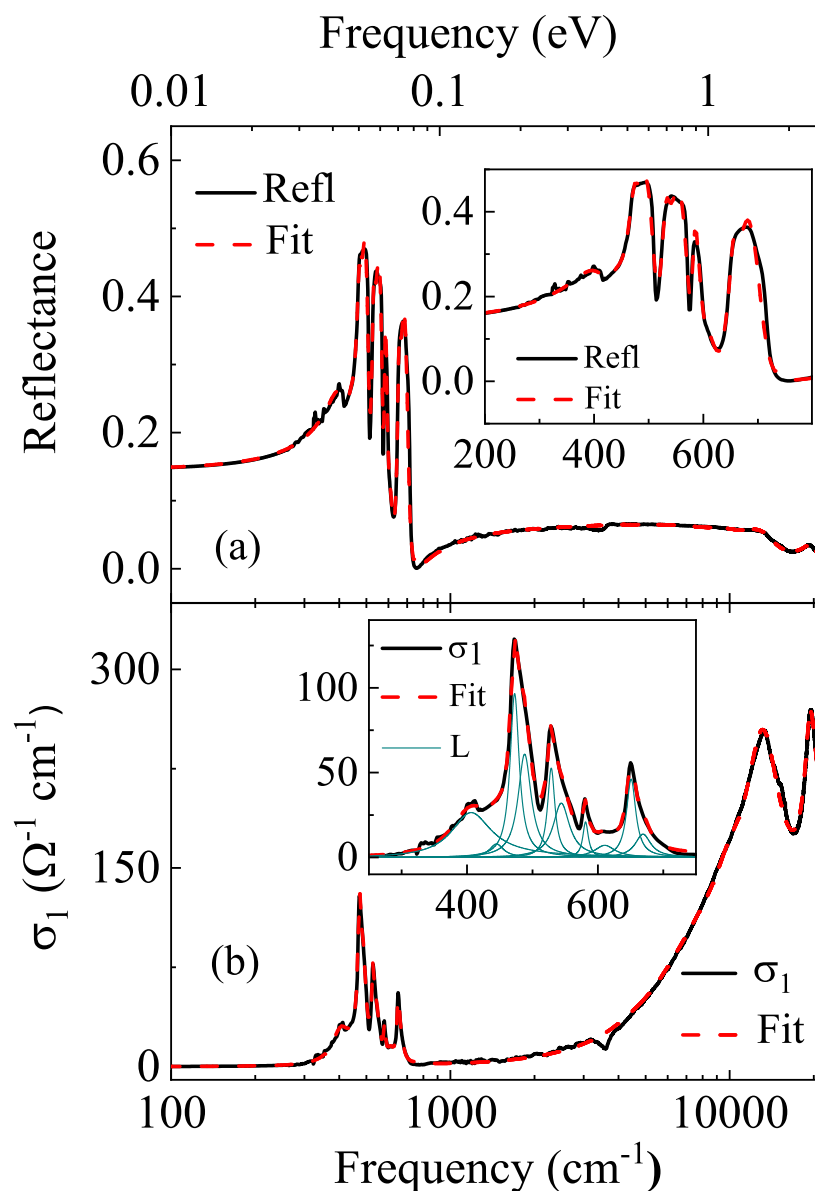
Figure 4. Ambient pressure (**a**) reflectance and (**b**) optical conductivity spectrum of $LiInCr_4O_8$ in the range 100–22,000 cm^{-1}, together with the Lorentz fitting. The insets of (**a**,**b**) depict the corresponding low-frequency range (200–800 cm^{-1}) of the reflectance and optical conductivity spectrum, respectively, where the phonon modes are located, together with the Lorentz fitting.

3.2. High-Pressure Results

3.2.1. X-ray Diffraction Measurements

A few XRD patterns at selected pressures are presented in Figure 5. According to these results, the sample remains in the ambient phase up to ~14 GPa. Above 10 GPa, i.e., beyond the hydrostatic pressure limits of the PTM used, the peaks at higher values of 2θ become weaker and undergo a pressure-induced broadening, thereby making it difficult to trace their behaviour precisely with pressure. However, the peaks at lower angles provide clear signatures of phase transitions. Above 10 GPa, the (200) and (220) reflections show a broadening. Beyond ~14 GPa, they undergo a splitting, which is an indication of a first-order structural phase transition to a high-pressure phase (HP-1). The clear splitting of these off-diagonal planes into two peaks while the diagonal planes (111) remain intact is an indication of a cubic-to-tetragonal structural phase transition. Previous temperature-dependent XRD studies on $LiMCr_4O_8$ (M = In, Ga, Fe) compounds have

reported a cubic-to-tetragonal phase transition at very low temperatures. Based on earlier reported studies, the HP-1 phase was indexed to a tetragonal structure (space group $I\bar{4}m2$) with two formula units per unit cell ($Z = 2$). The Rietveld refinement of our XRD data collected at $\sim$14.3 GPa indicated the coexistence of the ambient and HP-1 phases (see Figure 6). The refined lattice parameters of the HP-1 phase at $\sim$14 GPa are $a = 5.9030(26)$ Å, $c = 8.0681(60)$ Å, and $V = 281.13(22)$ Å^3, with $R_p = 0.038$ and $R_{wp} = 0.058$. The structural information from the Rietveld analysis for the coexisting ambient and the HP-1 phases are given in Table 5 and Table 6, respectively. This information is also shown in Figure 8. For both the ambient and HP-1 phases, the atomic positions and their occupations were not refined and are used as reported in earlier studies [5,8]. The structural refinement of the diffraction patterns above 14 GPa could not be performed; hence, only one data point of the HP-1 phase is shown in Figure 8. Detailed information regarding the coordination of polyhedral units cannot be extracted from this powder diffraction as the oxygen positions remain unrefined to maintain the reliability of the Rietveld refinement. The volume per formula unit in the ambient pressure phase is 148.38 Å^3 and that of the HP-1 phase is 140.57 Å^3, which gives a compression of 5.3% per formula unit.

Table 5. The Wyckoff sites, fractional coordinates, and occupations as reported in an earlier study [5] and the thermal parameter U as obtained from Rietveld refinement of LiInCr$_4$O$_8$ in the ambient structure at $\sim$14 GPa. Space group $F\bar{4}3m$, $Z = 4$, $a = 8.2624(13)$ Å and $V = 564.05(26)$ Å^3.

Atom	Wyckoff	x	y	z	Occupancy	U
Li1	4a	0.0000	0.0000	0.0000	0.9920	0.0610
In1	4a	0.0000	0.0000	0.0000	0.0080	0.0900
Li2	4d	0.7500	0.7500	0.7500	0.0080	0.8000
In2	4d	0.7500	0.7500	0.7500	0.9920	0.0636
Cr	16e	0.3719	0.3719	0.3719	1.0000	0.0064
O1	16e	0.1377	0.1377	0.1377	1.0000	0.0301
O2	16e	0.6107	0.6107	0.6107	1.0000	0.0671

Table 6. The Wyckoff sites, fractional coordinates, and occupations as reported in an earlier study [8] and the thermal parameter U as obtained from Rietveld refinement of LiInCr$_4$O$_8$ in the HP-1 phase at $\sim$14 GPa. Space group $I\bar{4}m2$, $Z = 2$, $a = 5.9030(26)$ Å, $c = 8.0681(60)$ Å, and $V = 281.13(22)$ Å^3.

Atoms	Wyckoff Sites	x	y	z	Occupancy	U
Li	2a	0.0000	0.0000	0.0000	1.0000	0.0224
In	2d	0.0000	0.5000	0.7500	1.0000	0.0875
Cr	8i	0.2607	0.0000	0.6272	1.0000	0.0067
O1	8i	0.2840	0.0000	0.6340	1.0000	0.0029
O2	8i	0.2510	0.0000	0.1080	1.0000	0.0069

The low-temperature XRD studies on LiInCr$_4$O$_8$ reported the tetragonal phase coexisting with the ambient cubic phase down to the lowest recorded temperature of $\sim$2 K [7,8]. Consistently, our high-pressure studies also show that the sample does not completely transform to the tetragonal phase with further compression. Instead, before this cubic to tetragonal transition is completed, the reflections from the (111) set of planes undergo a broadening at the next recorded pressure ($\sim$16 GPa) and then split into two peaks at higher pressures. The XRD pattern recorded at $\sim$19.7 GPa shows clear changes, indicating the existence of a new high-pressure phase (HP-2 phase). The transition from the HP-1 to HP-2 phase is a slow and sluggish first-order structural phase transition where the HP-1 coexists with the evolving HP-2 phase. This new high-pressure phase (HP-2 phase) remains stable up to $\sim$35 GPa. With further compression, the diffraction pattern recorded above $\sim$35 GPa shows the emergence of some new peaks, suggesting a possible transition to a lower-symmetry structure (HP-3 phase). The transition to the HP-3 phase was not completed at the highest pressure recorded in this experiment (i.e., $\sim$36.7 GPa). Due to

the broadness of the diffraction peaks, overlapping with the strong reflections from the pressure marker (Au) and the gasket (W) used in these experiments, the high-pressure phases could not be identified. During decompression, the HP-1 and HP-2 phases coexist down up to 12 GPa. Below 8 GPa, the sample slowly transforms to the parent phase and reverts to the ambient pressure crystal structure on complete release of pressure.
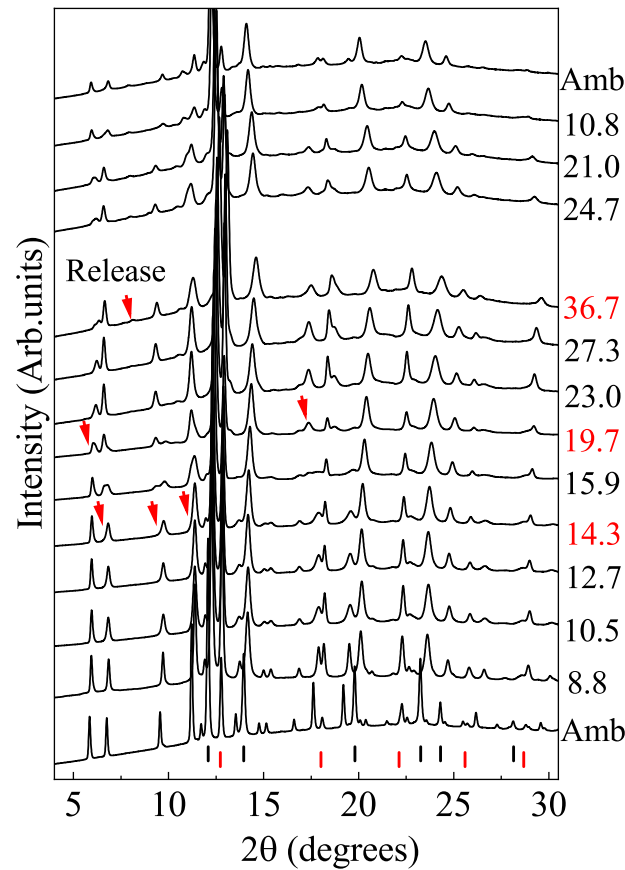

Figure 5. Pressure-dependent XRD patterns at few selected pressures. The pressure values on the right are in GPa. The red arrows indicate the emerging new reflections. The red and black ticks at the bottom are from Au (pressure marker) and W (gasket), respectively.
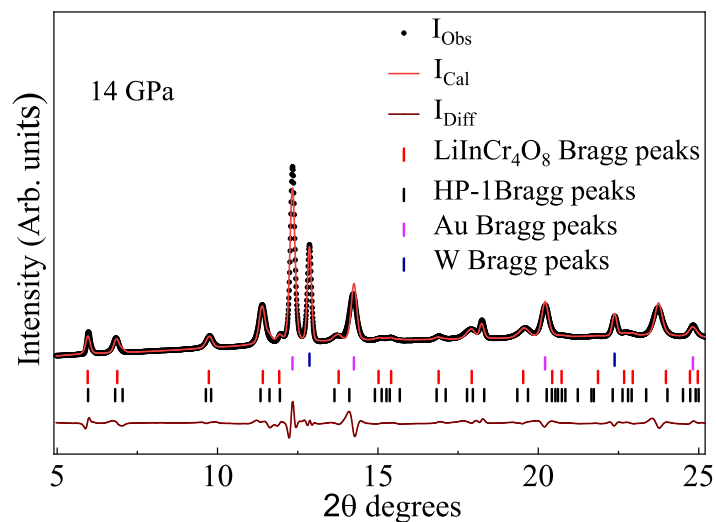
Figure 6. Rietveld refinement of the XRD pattern at ~14 GPa, demonstrating the coexistence of the HP-1 (space group I$\bar{4}$m2) phase with the ambient pressure cubic phase.

It is well known that the diffraction peak width has its origins from instruments, particle size, and stress-induced broadening. In this study, the XRD pattern from standard CeO_2 inside the DAC recorded at ambient conditions was used to characterize the instrumental broadening. Changes in the peak width under compression observed in the present study can be attributed to inhomogeneous strain and change in crystallinity due to phase transformation. For a better understanding of the deformation at high pressures, the behaviour of the diffraction peaks and X-ray peak broadening were studied by plotting the variation of the peak position and the full-width-at-half-maximum (FWHM) value for the reflections from the (111), (200), and (220) planes as a function of pressure in Figure 7a,b, respectively. Structural phase transitions to the HP-1, HP-2, and HP-3 phases at ~14 GPa, ~19 GPa, ~35 GPa, respectively, can be clearly observed from Figure 7b. The FWHM value of all peaks remains almost constant up to ~10 GPa. Above ~10 GPa, all the peaks show a slight discontinuity and broadening, which can be attributed to the non-hydrostatic stresses [38]. However, the (hk0) and (h00) peaks show a significant change in the FWHM as compared to the (111) set of planes. This sudden change is observed in FWHM just before the structural transition at ~14 GPa. Immediately after the phase transition, i.e., above ~14 GPa, both (220) and (200) undergo a clear splitting due to the transition from the cubic to tetragonal phase. Above ~16 GPa, the (111) reflection also shows a sudden change in FWHM, which is an indication of beginning of another structural transition. With further compression, the (111) reflection exhibits a clear splitting (see Figure 7a).
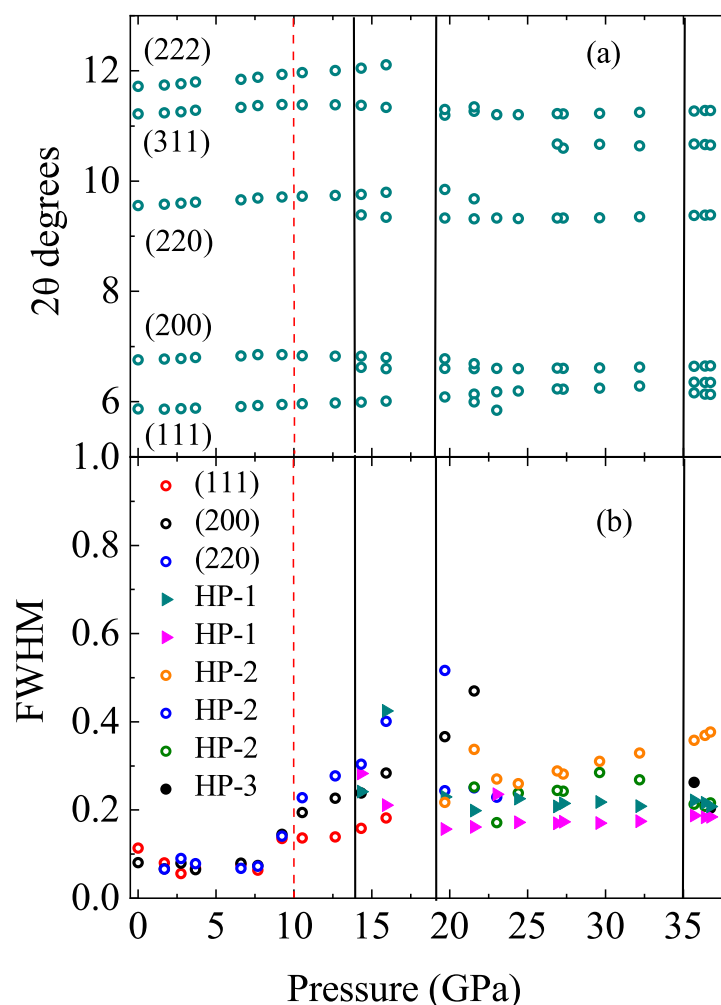

Figure 7. Behaviour of the (**a**) Bragg peaks and (**b**) FWHM with pressure. The vertical red dashed line indicates the hydrostatic limit of the PTM used. Solid black lines mark the transition pressures.

To determine the structural stability of $LiInCr_4O_8$, the lattice parameter a and the volume per unit cell V were determined for each recorded pressure from the structural refinements. Both parameters are plotted in Figure 8, where the abrupt decrease in compressibility is notable above $\sim$10 GPa due to nonhydrostatic conditions [39,40]. The P–V data up to $\sim$10 GPa (hydrostatic limit of PTM used) was fitted with a Murnaghan equation of state according to $V(p) = V_0 \cdot [(B'_0 / B_0) \cdot p + 1]^{-1/B'_0}$ [41], where the first-order derivative of the bulk modulus B'_0 was fixed to 4 (see Figure 8). The bulk modulus B_0 of the ambient phase was found to be 186.7 ± 6.1 GPa. From the DFT calculations, the ambient pressure crystal structure was relaxed at different target pressures. The energy per formula unit and the corresponding volumes were fitted with the Murnaghan equation of state to compare with the experimental findings. The calculated B_0 and B'_0 amount to 176.8 ± 0.1 GPa and 4.63 ± 0.02, respectively. The difference in the experimental and calculated ambient volume and the non-magnetic configuration of the calculated system could explain the discrepancy between the experimental and theoretical values of the bulk modulus.
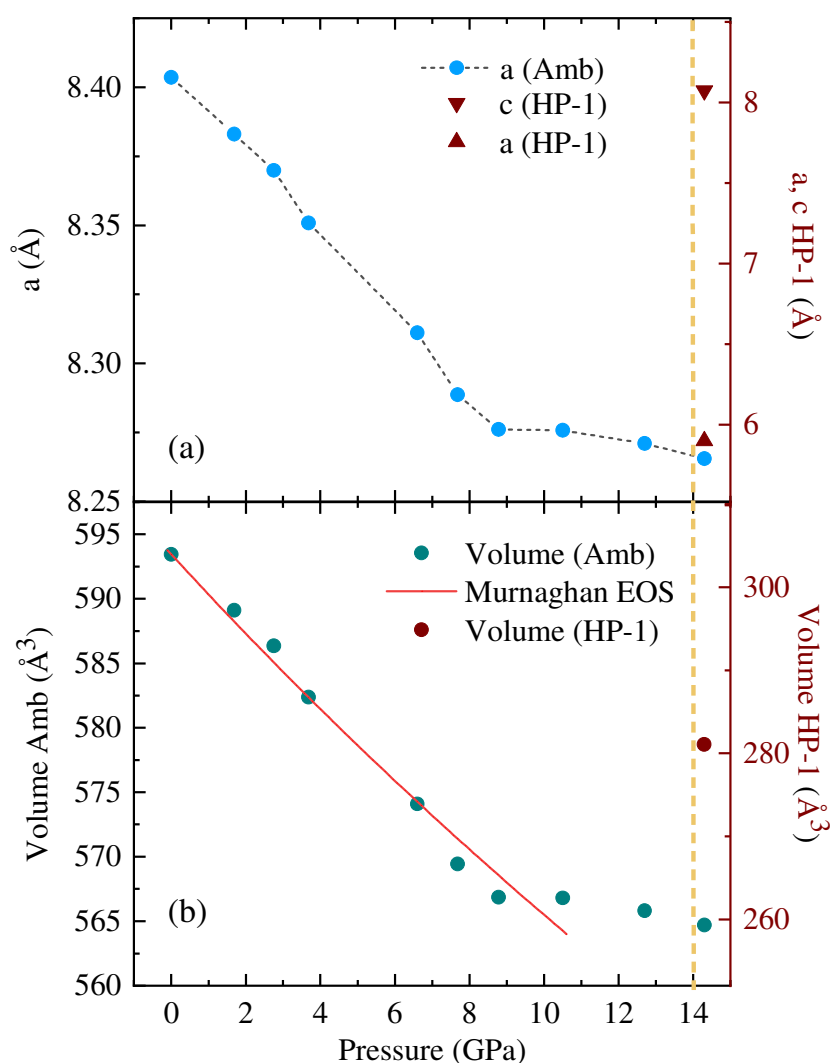

Figure 8. (**a**) Experimental lattice parameters a and c and (**b**) volume per unit cell V of the ambient phase and high-pressure HP-1 phase (scale on the right side of the graph) as a function of pressure. The pressure dependence of the volume is fitted with a Murnaghan equation of state (EOS), as defined in the text.

$LiInCr_4O_8$ with two different Cr–Cr distances (d = 2.90 Å and d' = 3.05 Å) has values that lie in the range of conventional spinels such as $ZnCr_2O_4$ with a uniform Cr–Cr

distance of 2.944 Å, and that of $CdCr_2O_4$ is 3.041 Å. A theoretical study on $MgCr_2O_4$, $MnCr_2O_4$, and $ZnCr_2O_4$ reports their bulk moduli to be 197.3 GPa, 205.8 GPa, and 215 GPa, respectively, [42], whereas experimentally, $MgCr_2O_4$ is reported to have a bulk modulus of 189 GPa [43,44] and that of $ZnCr_2O_4$ is 183.1 GPa [45]. $LiCrO_2$ is reported to have a bulk modulus of 161 GPa [46]. The experimentally obtained value of B_0 for $LiInCr_4O_8$ from the present study is comparable with that of other chromium spinels.

3.2.2. Raman Spectroscopy Measurements

To investigate the pressure-induced changes in the vibrational properties of $LiInCr_4O_8$, high-pressure Raman spectra were recorded in the spectral range $\sim$120–850 cm^{-1}. Figure 9 depicts Raman spectra at selected pressures. At the lowest recorded pressure of $\sim$0.4 GPa, the spectrum shows a splitting of a few Raman modes in the range of 450–600 cm^{-1}. Because the high-pressure XRD measurements do not provide any indication of a structural transition at such low pressures, the splitting of the Raman modes can be attributed to a loss of accidental degeneracy. All observed Raman modes shift to higher frequencies under pressure due to the pressure-induced stiffening of the lattice. The intensity of the Raman mode observed at $\sim$164 cm^{-1} drops drastically with compression, and this mode vanishes above $\sim$2.5 GPa. Mode M_2 at $\sim$310 cm^{-1} also undergoes a significant decrease in the intensity with pressure. Both these modes are associated with the translational motion of the A-site cations. The modes M_4 and M_6, which are related to the O–Li–O bending and O–In stretching vibrations, respectively, undergo a splitting at $\sim$ 0.4 GPa. The modes M_3 and M_4 combine into a single mode at $\sim$9 GPa. At $\sim$2.5 GPa, a further splitting of mode M_6 is observed, and this new mode can be traced up to $\sim$10 GPa. The splitting of modes associated with internal vibrations of polyhedral units can be attributed to the distortion under pressure. No significant changes in the Raman spectrum are observed with further compression up to $\sim$14 GPa. Above 14 GPa, the splitting of the mode at $\sim$545 cm^{-1} can be associated with the structural phase transition as observed from XRD measurements. The most intense mode (M_7), associated with the O–Cr–O bending vibrations, remains the most intense peak up to the highest recorded pressure of $\sim$ 18 GPa.

The frequency shift of the Raman modes with pressure is summarized in Figure 10, where the emerging new modes can be clearly seen. During pressure release (see Figure 9), the sample slowly reverts to its ambient pressure phase, where the modes at $\sim$310 cm^{-1} reappear at around 7 GPa, and the mode at $\sim$164 cm^{-1} can be observed at $\sim$3 GPa. According to the decompressed spectrum at ambient conditions, the sample has transformed to its ambient phase, consistent with our pressure-dependent XRD results.

The calculated pressure coefficients of Raman modes and the corresponding Grüneisen parameters ($\gamma_i = (B_0/\omega_i)(d\omega_i/dP)$) are tabulated in Table 7. B_0 is the experimentally obtained bulk modulus which was used to calculate the mode Grüneisen parameters for the ambient phase. The modes M_8 and M_9 show relatively larger value of the pressure coefficient, indicating an increase in the force constant under pressure. The tabulated mode Grüneisen parameter relates the vibrational properties to the crystal deformations. The macroscopic Grüneisen parameter γ is a weighted sum of individual γ_i's. The relation between the two is given as $[\gamma = (\sum_i \gamma_i C_i)/(\sum_i C_i)]$, where C_i's are the mode contributions to the material's specific heat [47]. Using Einstein's specific heat relation, $C_i = R[x_i^2 exp(x_i)]/[exp(x_i) - 1]^2$ (where $x_i = \hbar\omega_i/k_B T$ and R is the universal gas constant) [48], the macroscopic Grüneisen parameter was calculated using the observed modes from M_1 to M_9 at ambient pressure and its value was found to be $\gamma = 0.99$. A negative contribution to thermal expansion can be associated with a negative mode Grüneisen parameter. In the ambient phase, all the modes are notably contributing to a positive thermal expansion, consistent with recent studies [27,49] stating a positive expansion observed in $LiInCr_4O_8$, whereas other isostructural compounds $LiGaCr_4O_8$ and $LiInCr_4S_8$ are reported to exhibit negative thermal expansion. A softening of the M_{1-HP} mode is, however, observed in the high-pressure phase. All the other modes observed above 14 GPa still show a positive shift with compression.
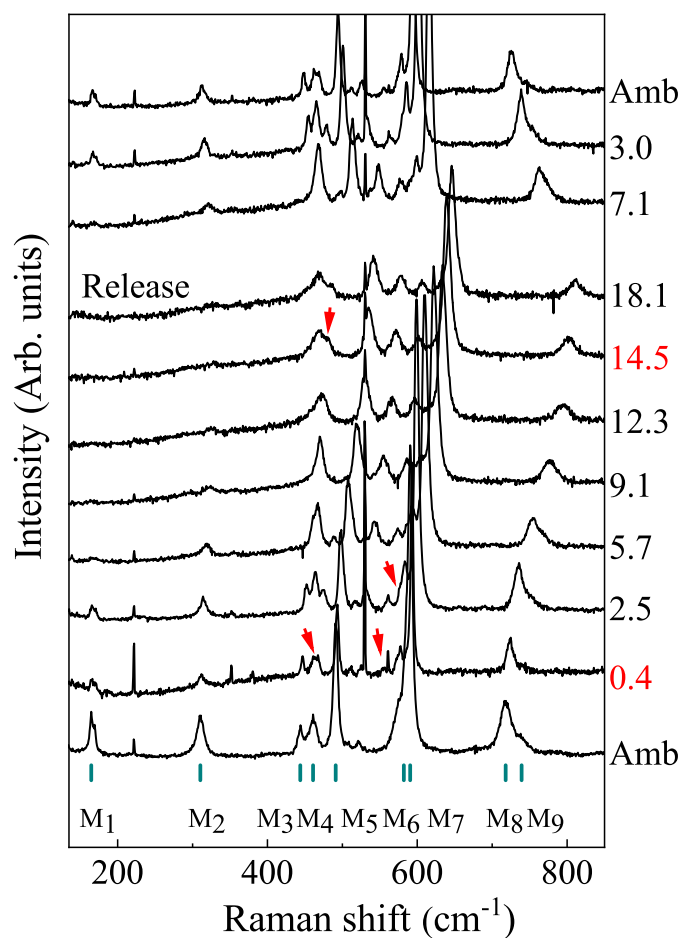
Figure 9. Raman spectra of $LiInCr_4O_8$ at selected pressures. The numbers on the right are in GPa scale. Red arrows indicate the emergence of new Raman modes.
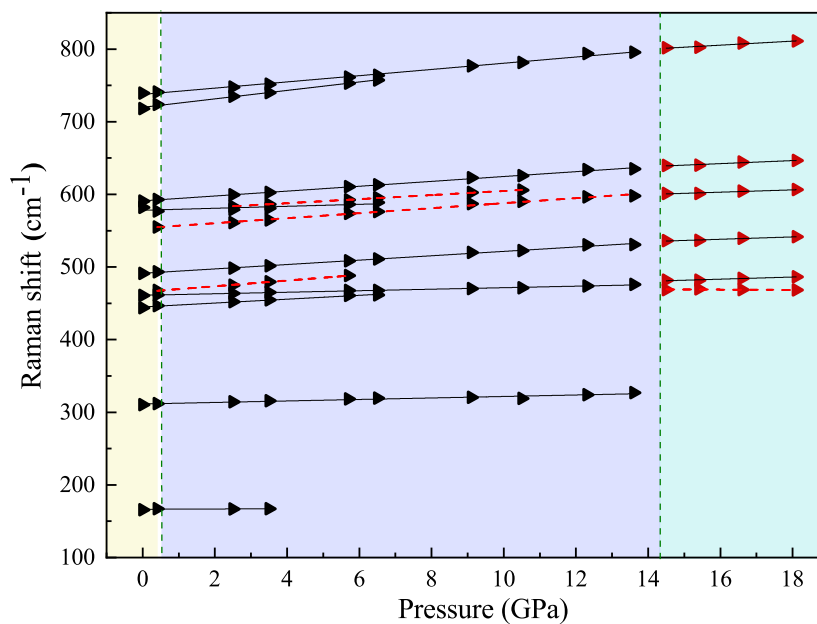

Figure 10. Frequency shift of Raman modes with increasing pressure. The black and red symbols represent the Raman modes of the ambient phase and those observed above 14 GPa, respectively. Different shadings illustrate the changes in the Raman spectrum. The red dashed lines highlight new modes emerging under pressure.

Table 7. Pressure at which the modes are observed, frequency ω_i of observed Raman modes, pressure coefficients $d\omega_i/dP$ of Raman modes, and mode Grüneisen parameter γ_i (see text).

Observed Pressure GPa	Modes	ω_i (cm^{-1})	$(d\omega_i/dP)$ (cm^{-1}GPa^{-1})	γ_i
Amb	M_1	165	0.21	0.23
"	M_2	310	0.90	0.51
"	M_3	444	2.67	1.06
"	M_4	461	0.04	0.40
"	M_5	491	3.02	1.09
"	M_6	582	1.36	0.41
"	M_7	591	3.35	1.00
"	M_8	718	5.82	1.43
"	M_9	739	4.28	1.02
0.4	M_{10}	468	3.92	1.48
0.4	M_{11}	555	3.45	1.10
2.5	M_{12}	584	2.81	0.85
14.5	M_{1-HP}	469	−0.25	−0.09
"	M_{2-HP}	482	1.47	0.54
"	M_{3-HP}	536	1.62	0.53
"	M_{4-HP}	601	1.59	0.47
"	M_{5-HP}	640	2.09	0.58
"	M_{6-HP}	802	2.79	0.62

3.2.3. Infrared Spectroscopy Measurements

The pressure dependence of the absorbance spectrum of LiInCr$_4$O$_8$ is depicted in Figure 11a for pressures up to ~17.4 GPa. The features observed close to 2000 cm^{-1} are due to the multi-phonon absorptions in diamond. In the recorded range, we observed four phonon modes at low frequencies followed by the onset of electronic transitions at around 1000 cm^{-1}. In comparison to the ambient pressure optical conductivity (Figure 4), the onset of electronic transitions is spread out in the absorption spectrum, and the crystal field excitation appears as a broad peak in the spectrum around 16,800 cm^{-1} (2.05 eV), corresponding to the spin-allowed intra-atomic *d-d* transition between the ground state $^4A_{2g}$ and the excited $^4T_{1g}$ and $^4T_{2g}$ states [28–32]. The pressure dependence of this onset is extracted by extrapolation of a linear fit for each pressure value up to 10 GPa (Figure 12b). Beyond this pressure, the change in the spectral slope leads to unrealistic values for linear extrapolation. The onset of electronic transitions shifts to higher energies with increasing pressure indicating an increase in the band gap under compression, in agreement with the pressure-induced blue-shift of the crystal field excitation (Figure 12b). The observed crystal field excitations were fitted to a Lorentzian profile to obtain the corresponding energy position. This result is consistent with an earlier reported infrared absorption study on CdCr$_2$O$_4$, where a similar behaviour of the crystal field excitation under pressure was observed [32]. Weak features slowly emerging close to ~14,500 cm^{-1} at 4.6 GPa (marked by black arrows in Figure 11a) can be ascribed to the spin-forbidden crystal field transitions that may become infrared-active as a result of lattice vibrations which locally break the centre of symmetry. The absorption spectrum at the highest pressure of ~17.4 GPa shows a changed crystal field excitation profile, which we relate to the pressure-induced structural phase transition observed at ~19 GPa in our XRD measurements. The slightly lower critical pressure extracted from our infrared studies can be explained by the solid PTM used, which is less hydrostatic than the PTM (alcohol mixture) of the XRD experiment [50,51].

The pressure-dependent frequencies of the infrared-active phonon modes are presented in Figure 12a. In this spectral region, the observed modes belong to the internal bending vibrations of the CrO$_6$ octahedral unit and Li–O stretching vibrations. The observed infrared-active modes show a blueshift under pressure, consistent with the pressure behaviour of the Raman modes. The phonon modes P$_1$ and P$_2$ merge at 14 GPa, whereas

the mode P_4 shows a deviation from a linear fit at the same pressure. At the same pressure, one observes a sudden change in the slope of the pressure-induced shift of the crystal field excitation (Figure 12b). All these changes can be associated with the structural phase transition observed from XRD measurements (discussed earlier). In Figure 12b, a sudden jump in the onset energy is also observed at 7.4 GPa; this, however, cannot be associated with any structural phase transition. The pressure coefficients $(d\omega/dP)$ of the observed $(P_1–P_4)$ modes are 5.1, 5.24, 4.28, and 3.69 $cm^{-1}GPa^{-1}$, respectively. These values are comparable and close to the pressure coefficients of the high-energy Raman modes (M_5, M_7, M_8, and M_9) (see Table 7).
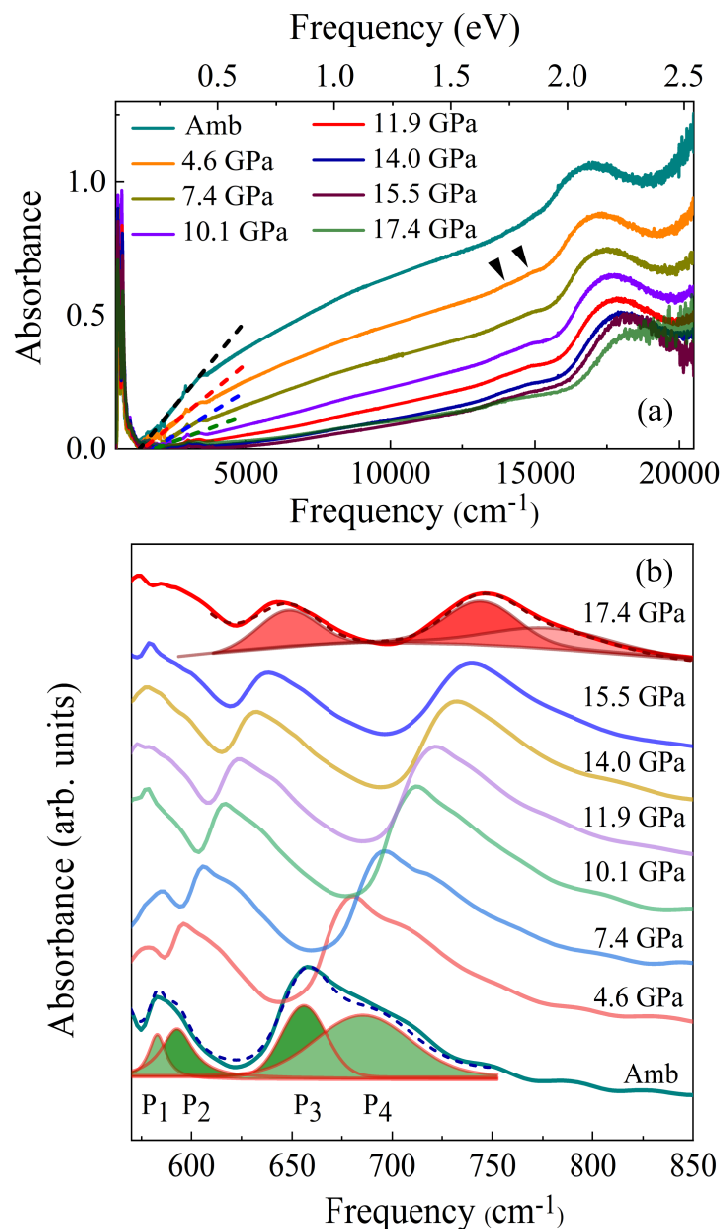
Figure 11. (**a**) Pressure-dependent infrared absorbance spectra in a broad frequency range 500–20,500 cm^{-1}. The two weak features indicated by black arrows are due to spin-forbidden crystal field excitations. (**b**) Low-frequency absorbance spectra with phonon modes (labelled P1–P4) as a function of pressure, fitted with Lorentz oscillators.
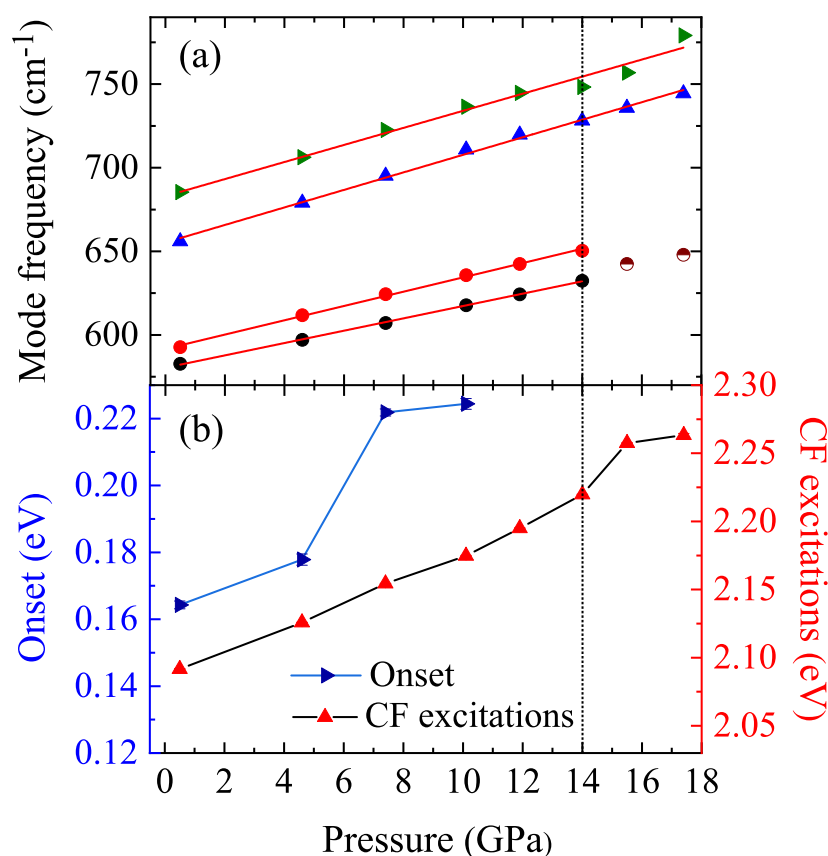
Figure 12. (**a**) Behaviour of infrared-active phonon mode frequencies with pressure. (**b**) Onset of electronic transitions and energy of crystal field (CF) excitation as a function of pressure. The vertical line at ∼14 GPa indicates the structural phase transition.

4. Conclusions

In summary, we report multiple pressure-induced phase transitions in the chromium spinel $LiInCr_4O_8$. From the high-pressure XRD measurements, the HP-1 phase with tetragonal structure appearing at ∼14 GPa seems to be an intermediate metastable phase. The system does not completely transform to this structure and always coexists with the ambient pressure cubic phase. The high-pressure infrared and Raman spectroscopy measurements confirm the structural phase transition at ∼14 GPa. All the observed active modes show a pressure-induced blueshift indicative of the stiffening of the lattice. The estimated onset of the electronic transitions from the high-pressure infrared measurements indicates an increase in the band gap under compression. Although the breathing pyrochlore structure of $LiInCr_4O_8$ is known to be a geometrically frustrated system, it appears to be highly resilient when the system reverts to its ambient phase even after undergoing multiple pressure-induced structural changes.

References

1. Zhao, Q.; Yan, Z.; Chen, C.; Chen, J. Spinels: Controlled Preparation, Oxygen Reduction/Evolution Reaction Application, and Beyond. *Chem. Rev.* **2017**, *117*, 10121–10211. [CrossRef] [PubMed]
2. Stefan, E.; Irvine, J.T.S. Synthesis and characterization of chromium spinels as potential electrode support materials for intermediate temperature solid oxide fuel cells. *J. Mater. Sci.* **2011**, *46*, 7191–7197. [CrossRef]
3. Kim, D.C.; Ihm, S.K. Application of Spinel-Type Cobalt Chromite as a Novel Catalyst for Combustion of Chlorinated Organic Pollutants. *Environ. Sci. Technol.* **2000**, *35*, 222–226. [CrossRef] [PubMed]
4. Joubert, J.C.; Durif, A. Étude de quelques composés spinelles nouveaux possédant un ordre des cations du type 1/1 sur les sites tétraédriques. *Bull. Soc. Française Min. Cristallogr.* **1966**, *89*, 26. [CrossRef]
5. Okamoto, Y.; Nilsen, G.J.; Attfield, J.P.; Hiroi, Z. Breathing Pyrochlore Lattice Realized in A-Site Ordered Spinel Oxides $LiGaCr_4O_8$ and $LiInCr_4O_8$. *Phys. Rev. Lett.* **2013**, *110*, 097203. [CrossRef] [PubMed]
6. Tanaka, Y.; Yoshida, M.; Takigawa, M.; Okamoto, Y.; Hiroi, Z. Novel Phase Transitions in the Breathing Pyrochlore Lattice: Li-NMR7 on $LiInCr_4O_8$ and $LiGaCr_4O_8$. *Phys. Rev. Lett.* **2014**, *113*, 227204. [CrossRef]
7. Nilsen, G.J.; Okamoto, Y.; Masuda, T.; Carvajal, J.R.; Mutka, H.; Hansen, T.; Hiroi, Z. Complex magnetostructural order in the frustrated spinel $LiInCr_4O_8$. *Phys. Rev. B* **2015**, *91*, 174435. [CrossRef]
8. Saha, R.; Fauth, F.; Avdeev, M.; Kayser, P.; Kennedy, B.J.; Sundaresan, A. Magnetodielectric effects in A-site cation-ordered chromate spinels $LiMCr_4O_8$ (M=Ga and In). *Phys. Rev. B* **2016**, *94*, 064420. [CrossRef]
9. Saha, R.; Dhanya, R.; Bellin, C.; Béneut, K.; Bhattacharyya, A.; Shukla, A.; Narayana, C.; Suard, E.; Carvajal, J.R.; Sundaresan, A. Magnetostructural coupling and magnetodielectric effects in the A -site cation-ordered spinel $LiFeCr_4O_8$. *Phys. Rev. B* **2017**, *96*, 214439. [CrossRef]
10. Dewaele, A.; Loubeyre, P.; Mezouar, M. Equations of state of six metals above 94 GPa. *Phys. Rev. B* **2004**, *70*, 094112. [CrossRef]
11. Takemura, K.; Dewaele, A. Isothermal equation of state for gold with a He-pressure medium. *Phys. Rev. B* **2008**, *78*, 104119. [CrossRef]
12. Klotz, S.; Chervin, J.C.; Munsch, P.; Marchand, G.L. Hydrostatic limits of 11 pressure transmitting media. *J. Phys. D Appl. Phys* **2009**, *42*, 075413. [CrossRef]
13. Hammersley, A.P.; Svensson, S.O.; Hanfland, M.; Fitch, A.N.; Hausermann, D. Two-dimensional detector software: From real detector to idealised image or two-theta scan. *High Press. Res.* **1996**, *14*, 235. [CrossRef]
14. Toby, B.H. EXPGUI, a graphical user interface for GSAS. *J. Appl. Crystallogr.* **2001**, *34*, 210. [CrossRef]
15. Mao, H.K.; Xu, J.; Bell, P.M. Calibration of the ruby pressure gauge to 800 kbar under quasi-hydrostatic conditions. *J. Geophys. Res.* **1986**, *91*, 4673. [CrossRef]
16. Celeste, A.; Borondics, F.; Capitani, F. Hydrostaticity of pressure-transmitting media for high pressure infrared spectroscopy. *High Press. Res.* **2019**, *39*, 608. [CrossRef]
17. Blöchl, P.E. Projector augmented-wave method. *Phys. Rev. B* **1994**, *50*, 17953. [CrossRef]
18. Giannozzi, P.; Andreussi, O.; Brumme, T.; Bunau, O.; Nardelli, M.B.; Calandra, M.; Car, R.; Cavazzoni, C.; Ceresoli, D.; Cococcioni, M.; et al. Advanced capabilities for materials modelling with Quantum ESPRESSO. *J. Condens. Matter Phys.* **2017**, *29*, 465901. [CrossRef]
19. Perdew, J.P.; Burke, K.; Ernzerhof, M. Generalized Gradient Approximation Made Simple. *Phys. Rev. Lett.* **1996**, *77*, 3865. [CrossRef]
20. Monkhorst, H.J.; Pack, J.D. Special points for Brillouin-zone integrations. *Phys. Rev. B* **1976**, *13*, 5188. [CrossRef]
21. Lazzeri, M.; Mauri, F. First-Principles Calculation of Vibrational Raman Spectra in Large Systems: Signature of Small Rings in CrystallineSiO_2. *Phys. Rev. Lett.* **2003**, *90*, 036401. [CrossRef] [PubMed]
22. Troullier, N.; Martins, J.L. Efficient pseudopotentials for plane-wave calculations. *Phys. Rev. B* **1991**, *43*, 1993. [CrossRef] [PubMed]
23. Mougin, J.; LeBihan, T.; Lucazeau, G. High-pressure study of Cr2O3 obtained by high-temperature oxidation by X-ray diffraction and Raman spectroscopy. *J. Phys. Chem. Solids* **2001**, *62*, 553. [CrossRef]
24. Todorov, N.D.; Abrashev, M.V.; Russev, S.C.; Marinova, V.; Nikolova, R.P.; Shivachev, B.L. Raman spectroscopy and lattice-dynamical calculations of Sc_3CrO_6 single crystals. *Phys. Rev. B* **2012**, *85*, 214301. [CrossRef]
25. Feng, Y.; Liu, H.; Bian, J.; Xiong, W.; Zhu, S.; Zong, B.; Shi, B.; Fang, B. Structural and Magnetic Properties of the Breathing Pyrochlore $LiInCr_{4-x}Fe_xO_8$. *Phys. Status Solidi B* **2020**, *257*, 1900685. [CrossRef]

26. Schaftenaar, G.; Noordik, J.H. Molden: A pre- and post-processing program for molecular and electronic structures. *J. Comput. Aided Mol. Des.* **2000**, *14*, 123. [CrossRef] [PubMed]

27. Pokharel, G.; May, A.F.; Parker, D.S.; Calder, S.; Ehlers, G.; Huq, A.; Kimber, S.A.J.; Arachchige, H.S.; Poudel, L.; McGuire, M.A.; et al. Negative thermal expansion and magnetoelastic coupling in the breathing pyrochlore lattice material LiGaCr$_4$S$_8$. *Phys. Rev. B* **2018**, *97*, 134117. [CrossRef]

28. Ohgushi, K.; Okimoto, Y.; Ogasawara, T.; Miyasaka, S.; Tokura, Y. Magnetic, Optical, and Magnetooptical Properties of Spinel-Type ACr$_2$X$_4$ (A = Mn, Fe, Co, Cu, Zn, Cd : X = O, S, Se). *J. Phys. Soc. Japan* **2008**, *77*, 034713. [CrossRef]

29. Brik, M.; Avram, N.M.; Avram, C.N. Crystal field analysis of energy level structure of the Cr$_2$O$_3$ antiferromagnet. *Solid State Commun.* **2004**, *132*, 831. [CrossRef]

30. Brik, M. Crystal Field Analysis, Electron-Phonon Coupling and Spectral Band Shape Modeling in MgO:Cr$_3$. *Z. Naturforschung A* **2005**, *60*, 437. [CrossRef]

31. Larsen, P.K.; Wittekoek, S. Photoconductivity and Luminescence Caused by Band-Band and by Cr$_3$ Crystal Field Absorptions in CdCr$_2$S$_4$. *Phys. Rev. Lett.* **1972**, *29*, 1597. [CrossRef]

32. Rabia, K.; Baldassarre, L.; Deisenhofer, J.; Tsurkan, V.; Kuntscher, C.A. Evolution of the optical properties of chromium spinels CdCr$_2$O$_4$, HgCr$_2$S$_4$ and ZnCr$_2$Se$_4$ under high pressure. *Phys. Rev. B* **2014**, *89*, 125107. [CrossRef]

33. Schmidt, M.; Wang, Z.; Kant, C.; Mayr, F.; Toth, S.; Islam, A.T.M.N.; Lake, B.; Tsurkan, V.; Loidl, A.; Deisenhofer, J. Exciton-magnon transitions in the frustrated chromium antiferromagnets CuCrO$_2$,α-CaCr$_2$O$_4$, CdCr$_2$O$_4$, and ZnCr$_2$O$_4$. *Phys. Rev. B* **2013**, *87*, 224424. [CrossRef]

34. Rudolf, T.; Kant, C.; Mayr, F.; Schmidt, M.; Tsurkan, V.; Deisenhofer, J.; Loidl, A. Optical properties of ZnCr$_2$Se$_4$. *Eur. Phys. J. B* **2009**, *68*, 153. [CrossRef]

35. Figgis, B.N.; Hitchman, M.A. *Ligand Field Theory*; John Wiley & Sons: Hoboken, NJ, USA, 1999.

36. Jórgensen, C.K. Spectra and electronic structure of complexes with sulphur-containing ligands. *Inorg. Chim. Acta. Rev.* **1968**, *2*, 65. [CrossRef]

37. Tarte, P. Effet isotopique ^{6}Li-^{7}Li dans le spectre infra-rouge de composes inorganiques du lithium-I. Carbonate, chromo-ferrite, tungstate, molybdate et nitrate de lithium. *Spectrochim. Acta* **1965**, *21*, 313. [CrossRef]

38. Garg, A.B.; Errandonea, D.; Rodríguez-Hernández, P.; Muñoz, A. ScVO$_4$ under non-hydrostatic compression: A new metastable polymorph. *J. Phys. Condens. Matter* **2016**, *29*, 055401. [CrossRef] [PubMed]

39. Garg, A.B.; Errandonea, D.; Rodríguez-Hernández, P.; López-Moreno, S.; Muñoz, A.; Popescu, C. High-pressure structural behaviour of HoVO$_4$: Combined XRD experiments and *abinitio* calculations. *J. Phys. Condens. Matter* **2014**, *26*, 265402. [CrossRef] [PubMed]

40. Errandonea, D.; Muñoz, A.; Gonzalez-Platas, J. Comment on "High-pressure x-ray diffraction study of YBO$_3$/Eu^{3+}, GdBO$_3$ and EuBO$_3$" [J. Appl. Phys. 115, 043507 (2014)]. *J. Appl. Phys.* **2014**, *115*, 216101. [CrossRef]

41. Murnaghan, F.D. The Compressibility of Media under Extreme Pressures. *Proc. Natl. Acad. Sci. USA* **1944**, *30*, 244. [CrossRef]

42. Catti, M.; Fava, F.F.; Zicovich, C.; Dovesi, R. High-pressure decomposition of MCr$_2$O$_4$ spinels (M = Mg, Mn, Zn) by ab initio methods. *Phys. Chem. Miner.* **1999**, *26*, 389. [CrossRef]

43. Yong, W.; Botis, S.; Shieh, S.R.; Shi, W.; Withers, A.C. Pressure-induced phase transition study of magnesiochromite (MgCr$_2$O$_4$) by Raman spectroscopy and X-ray diffraction. *Phys. Earth Planet. Inter.* **2012**, *196–197*, 75. [CrossRef]

44. Wang, Z.; OŃeill, H.; Lazor, P.; Saxena, S.K. High pressure Raman spectroscopic study of spinel MgCr$_2$O$_4$. *J. Phys. Chem. Solids* **2002**, *63*, 2057. [CrossRef]

45. Wang, Z.; Lazor, P.; Saxena, S.K.; Artioli, G. High-Pressure Raman Spectroscopic Study of Spinel (ZnCr$_2$O$_4$). *J. Solid State Chem.* **2002**, *165*, 165. [CrossRef]

46. Garg, A.; Errandonea, D.; Pellicer-Porres, J.; Martinez-Garcia, D.; Kesari, S.; Rao, R.; Popescu, C.; Bettinelli, M. LiCrO$_2$ Under Pressure: In-Situ Structural and Vibrational Studies. *Crystals* **2018**, *9*, 2. [CrossRef]

47. Liu, G.; Gao, Z.; Ren, J. Anisotropic thermal expansion and thermodynamic properties of monolayer β-Te. *Phys. Rev. B* **2019**, *99*, 195436. [CrossRef]

48. Kamali, K.; Ravindran, T.R.; Ravi, C.; Sorb, Y.; Subramanian, N.; Arora, A.K. Anharmonic phonons of NaZr$_2$(PO$_4$)$_3$ studied by Raman spectroscopy, first-principles calculations, and x-ray diffraction. *Phys. Rev. B* **2012**, *86*, 144301. [CrossRef]

49. Kanematsu, T.; Mori, M.; Okamoto, Y.; Yajima, T.; Takenaka, K. Thermal Expansion and Volume Magnetostriction in Breathing Pyrochlore Magnets LiACr$_4$X$_8$ (A = Ga, In, X = O, S). *J. Phys. Soc. Japan* **2020**, *89*, 073708. [CrossRef]

50. Liang, A.; Turnbull, R.; Bandiello, E.; Yousef, I.; Popescu, C.; Hebboul, Z.; Errandonea, D. High-Pressure Spectroscopy Study of Zn(IO$_3$)$_2$ Using Far-Infrared Synchrotron Radiation. *Crystals* **2020**, *11*, 34. [CrossRef]

51. Kuntscher, C.A.; Pashkin, A.; Hoffmann, H.; Frank, S.; Klemm, M.; Horn, S.; Schönleber, A.; van Smaalen, S.; Hanfland, M.; Glawion, S.; et al. Mott-Hubbard gap closure and structural phase transition in the oxyhalides TiOBr and TiOCl under pressure. *Phys. Rev. B* **2008**, *78*, 035106. [CrossRef]